International Journal of Innovative Computing, Information and Control
Volume **21**, Number **5**, October **2025**

ICIC International ©2025 ISSN 1349-4198
pp. 1221–1237

A STUDY ON OUTPUT VOLTAGE STABILITY IN WIRELESS CHARGING SYSTEM BASED ON SLIDING MODE CONTROL

Wenzhou Lu[1,*], Xu Wu[1], Yixin Zhu[1], Tinglong Pan[1] and Dezhi Xu[2]

[1]School of Internet of Things Engineering
Jiangnan University
No. 1800, Lihu Avenue, Wuxi 214122, P. R. China
6221915024@stu.jiangnan.edu.cn; { yixinzhu1987; tlpan }@jiangnan.edu.cn
[*]Corresponding author: ewlu@jiangnan.edu.cn

[2]School of Electrical Engineering
Southeast University
No. 2, Sipailou, Xuanwu District, Nanjing 210096, P. R. China
xudezhi@seu.edu.cn

Received January 2025; revised April 2025

Abstract. *Wireless Power Transfer (WPT) eliminates the need for physical electrical connections, enabling the transmission of electrical energy from the power source to the load. The control of output voltage in WPT systems has been a major research focus. This paper investigates the Inductor-Capacitor-Capacitor-Series (LCC-S) wireless charging topology in combination with a synchronous BUCK converter, and proposes a Sliding Mode Control (SMC) strategy to regulate the output voltage in this scenario. First, the overall structure of the WPT system is analyzed, and the mathematical characteristics of the LCC-S topology are derived. The mathematical model of the synchronous BUCK converter is then developed, and the sliding mode surface along with the SMC law is designed based on this model. The stability of the SMC system is verified using the Lyapunov function. Finally, simulations are performed under four different operating conditions, with the results demonstrating that the proposed SMC system outperforms traditional PI control in terms of faster response speed, stronger disturbance immunity, smaller overshoot, and higher steady-state accuracy.*

Keywords: Wireless power transfer, Synchronous BUCK converter, Sliding mode control, PI control, LCC-S topology

1. **Introduction.** WPT represents a novel technology that facilitates the transmission of electrical energy from the power source to the load via magnetic field coupling [1]. In contrast to conventional wired charging methods, WPT offers several advantages, including enhanced safety, increased reliability, extended operational lifespan, and greater convenience [2-4]. These benefits have facilitated its widespread adoption in applications like Electric Vehicles (EVs), Autonomous Underwater Vehicles (AUVs), and Automated Guided Vehicles (AGVs) [5,6].

The stability and accuracy of the output voltage in a WPT system are crucial factors influencing the system's efficient operation. Throughout the charging process, variations in coil calibration, transmission distance, and load fluctuations can impact the extent of electromagnetic coupling, resulting in output voltage fluctuations. Inadequate control of the output voltage may lead to a range of adverse effects on the system's operation, including reduced charging efficiency, decreased equipment lifespan, and, in severe cases, potential safety risks such as personal injury. Therefore, the ability to maintain precise

---

DOI: 10.24507/ijicic.21.05.1221

regulation of the output voltage is directly correlated with the effectiveness of WPT system and the overall user experience [7-9].

To regulate the output voltage in a WPT system, a commonly employed approach is to incorporate a DC/DC converter between the receiver coil and the load, followed by closed-loop control of the output voltage. Cai et al. [10] achieve voltage regulation by monitoring the output equivalent impedance in real time and adjusting the duty cycle of a BUCK converter using PID control. In [11,12], constant voltage or constant current charging is maintained under load variations by cascading a DC/DC converter at the output side and employing PI control. In [13], a BUCK-BOOST converter is cascaded after a diode rectifier on the secondary side to achieve a controllable output voltage, thus enabling voltage regulation across a broader range of mutual inductance variations and input resistance. In [14], voltage control is realized by inserting a Battery Management Converter (BMC) in series on the secondary side. This approach is straightforward to implement and does not require a communication link, although it increases system size, and the BMC essentially functions as a DC/DC converter. In [15], output voltage regulation is achieved through load-independent Pulse Density Modulation (PDM). During constant voltage operation, the system maintains stable output by dynamically adjusting switching duty cycles in response to real-time load variations. In [16], an adaptive feed-forward control is introduced in the user-side buck converter for voltage regulation. By systematically analyzing system disturbances and dynamically adjusting the feed-forward gain, this method achieves rapid output voltage control while maintaining system stability. [17] presents a Model Predictive Control (MPC) approach for receiver-side DC-DC converters in wireless power transfer systems. The MPC algorithm, based on an accurate system model incorporating input voltage, output current, and parameter variations, outperforms traditional double closed-loop PID control in dynamic tracking performance, while requiring consideration of sampling delay effects on output accuracy. In [18], output voltage regulation is achieved through precise control of switching device conduction times. During constant voltage operation, the system dynamically adjusts the switching conduction angle based on power factor correction calculations and feedback signals, while maintaining stability despite measurement challenges in critical parameters such as inductance and capacitance. However, this is not easily achievable. Similarly, [19] proposes a variable inductance control method stabilizes output voltage/current through DC bias current adjustment, achieving near-zero phase angle impedance and constant current/voltage charging across wide coupling variations without auxiliary circuits. In [20], a hybrid control strategy combining modified asynchronous voltage cancellation and half-bridge modes enables zero-voltage switching across wide load ranges. This approach achieves constant current and constant voltage outputs through fixed frequency phase-shift control, eliminating the need for complex control algorithms or additional auxiliary circuits.

In addition to secondary-side control, primary-side control has gained significant attention in WPT systems. In [21], real-time output voltage monitoring enables constant voltage regulation through primary-side frequency control, eliminating the need for a back-end converter. In [22], online load identification is performed by collecting voltage and current data from the transmitter coil, which is then used to adjust the duty cycle of the primary-side DC/DC converter and inverter, ensuring voltage regulation. In [23], mutual inductance is monitored in real time by utilizing the relationship between inverter output current and mutual inductance, enabling automatic identification and maintaining a constant output voltage through phase shift control. To mitigate delays caused by high-speed wireless communication, [24] introduces an online Recursive Least Squares (RLS) filter for precise mutual inductance estimation, requiring only low-speed communication and enhancing system robustness. In [25], SMC is applied for output voltage regulation in an LCL-S topology WPT system. This method collects load voltage and filter capacitor current at the receiver side, calculates the phase shift angle, and controls the output voltage, offering superior robustness and dynamic performance over traditional PI control, though it still relies on a communication link. In [26,27], the output voltage can be precisely regulated by dynamically adjusting the switching frequency in response to variations in load resistance. In [28], a control method for submarine wireless power transfer systems is proposed, integrating frequency tracking with constant voltage/current charging modes. The frequency tracking regulates DC output through phase offset adjustment, while the constant voltage/current charging modes maintains stable output despite load impedance variations. In order to realize the regulation and control of the output voltage, [29] proposes a primary-side linear control strategy for output voltage regulation using LCC-N compensation topology. The strategy establishes load parameters, models the linear voltage-current relationship based on LCC-N characteristics, and achieves voltage control through fundamental and third harmonic waveform superposition.

Building on previous research, this paper proposes a sliding mode controller for the LCC-S topology combined with a synchronous BUCK converter to address the challenge of output voltage regulation in WPT systems. The proposed control strategy effectively suppresses disturbances and mitigates the effects of coils movement, demonstrating robust performance and accurate output voltage control. The effectiveness of the proposed strategy is validated through simulation and comparative experiments conducted in MATLAB/Simulink. This work presents the following contributions compared to the prior studies.

1) SMC is incorporated into the LCC-S topology combined with a synchronous BUCK converter, with the sliding mode surface and control law designed for the specific application scenario. The stability of the SMC system is then verified.

2) The proposed control strategy allows for secondary-side control without requiring communication between the primary and secondary sides, nor the need for complex algorithms.

3) Compared to conventional PI control, the proposed control strategy demonstrates superior robustness, faster dynamic response, enhanced steady-state accuracy, and stronger immunity to disturbances.

The paper is organized as follows. Section 2 presents a comprehensive analysis of the WPT system architecture and the LCC-S topology characteristics. Section 3 derives the mathematical model of the synchronous BUCK converter and designs the sliding mode controller. In Section 4, the proposed method is rigorously evaluated through simulations and compared with conventional PI control under four operating conditions, demonstrating its superior performance. Finally, Section 5 concludes the paper.

2. **Comprehensive Analysis of WPT System.**

In this section, the circuit structure of the WPT system is examined, and the characteristics of the LCC-S topology are analyzed.

2.1. **Architecture of WPT system.**

The overall circuit structure of the WPT system is shown in Figure 1, consisting of primary and secondary circuits. The primary side includes diodes D_1-D_4 for the industrial frequency mains rectifier, C_{in} as the Power Factor Correction (PFC) input capacitance, L_1 as the boost inductor, D_{g1} as the boost diode, D_{g2} as the protection diode, Q_{pfc} as the switching transistor, and C_1 as the PFC output capacitance, forming the BOOST-type PFC circuit. The primary-side full-bridge inverter consists of MOSFETs Q_1-Q_4. The LCC-type resonance compensation circuit includes L_{ps}, C_{pp}, and C_{ps}, along with L_p, the transmitter coil inductance. On the secondary side, L_s is the receiver coil inductance and C_s is the series compensation capacitance, forming

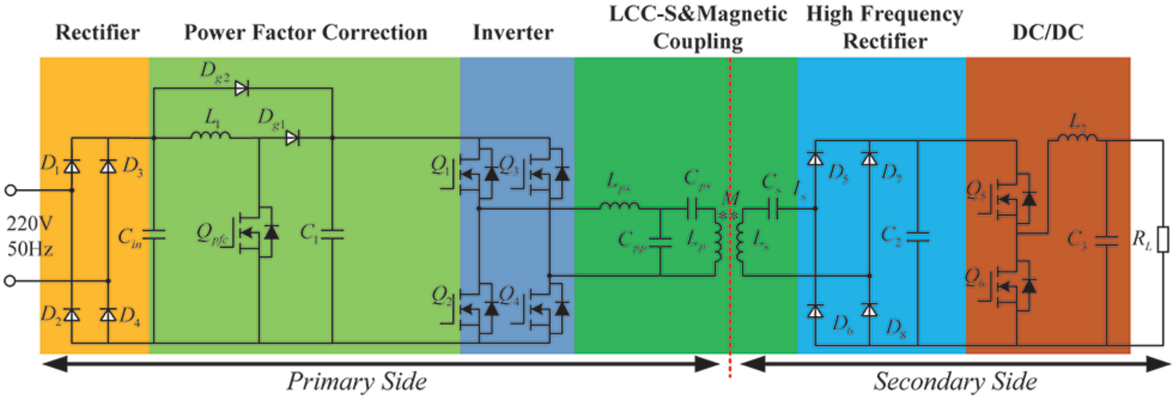

FIGURE 1. Overall circuit structure of the WPT system

the S-type resonance circuit. Diodes D_5-D_8 are high-frequency rectifiers, and MOSFETs Q_5-Q_6 are part of the DC/DC converter. L_2 is the energy storage inductor, C_3 is the output filter capacitor, and R_L is the system load.

On the primary side, 220 V industrial frequency utility power is rectified and processed by the PFC circuit to convert AC to DC and correct the grid current. The PFC circuit outputs a smooth 400 V DC, which is then supplied to the inverter to generate a high-frequency square wave. This high-frequency square wave is filtered by the resonance compensation circuit on the primary side to produce a high-frequency sinusoidal waveform, which is fed into the transmitter coil L_p as an excitation signal. Through electromagnetic induction, a sinusoidal signal of the same frequency is induced in the receiver coil L_s. This signal is rectified and filtered, then supplied to the DC/DC chopper circuit to provide a constant voltage output to the load.

2.2. **Topological characteristics of LCC-S.** The topology of the LCC-S circuit is shown in Figure 2. In this configuration, L_{ps}, L_p, and L_s represent the series resonant inductance on the primary side, the equivalent inductance of the transmitter coil, and the equivalent inductance of the receiver coil, respectively. R_{ps}, R_p, R_s, and R_L represent the parasitic resistances of the series inductor on the primary side, the transmitter coil, the receiver coil, and the equivalent load on the secondary side output, respectively. C_{pp}, C_{ps} and C_s correspond to the parallel resonant capacitance on the primary side, the series resonant capacitance, and the resonant capacitance on the secondary side. I_{in}, I_p, and I_s are the input current, the current through the transmitter coil, and the current through the receiver coil, respectively. U_{in} and U_o represent the output voltages of the inverter and the secondary side. M denotes the mutual inductance between the transmitter and receiver coils. On the primary side, L_{ps}, C_{pp}, C_{ps}, and L_p form the LCC structure, while L_s and C_s define the S-type structure on the secondary side.

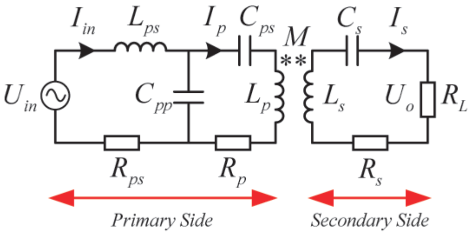

FIGURE 2. Structure of LCC-S topology

An equivalent mutual inductance circuit for the LCC-S topology is shown in Figure 3, where Z_{in} is the input equivalent impedance on the primary side of the LCC-S; Z_r is the equivalent impedance on the secondary side reflected to the primary side; and Z_s is the equivalent impedance on the secondary side.

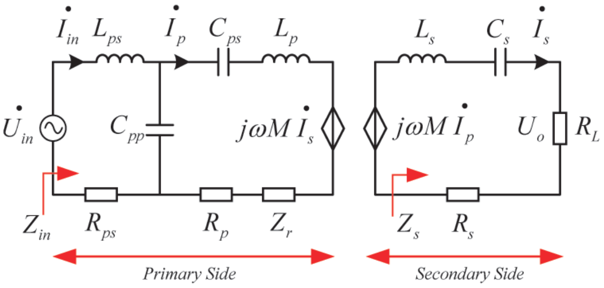

FIGURE 3. Equivalent mutual inductance circuit of LCC-S

Construct the voltage loop equation for the circuit based on Kirchhoff's voltage law, as shown in the following equation:

$$\begin{aligned} U_{in} &= j\omega I_{in}L_{ps} + \left(j\omega L_p + \frac{1}{j\omega C_{ps}} + R_p\right) I_p + R_{ps}I_{in} - j\omega MI_s \\ 0 &= \left(j\omega L_s + \frac{1}{j\omega C_s} + R_s + R_L\right) I_s - j\omega MI_p \end{aligned} \tag{1}$$

For the LCC-S topology to maintain resonant operation, the following fundamental conditions must be satisfied:

$$\begin{aligned} & j\omega L_{ps} + \frac{1}{j\omega C_{pp}} = 0 \\ & j\omega L_p + \frac{1}{j\omega C_{ps}} + \frac{1}{j\omega C_{pp}} = 0 \\ & j\omega L_s + \frac{1}{j\omega C_s} = 0 \end{aligned} \tag{2}$$

The equivalent impedance Z_s on the secondary side is

$$Z_s = j\omega L_s + \frac{1}{j\omega C_s} + R_s + R_L \tag{3}$$

The equivalent impedance Z_r reflected from the secondary side to the primary side is

$$Z_r = \frac{\omega^2 M^2}{R_s + R_L + j\omega L_s + \frac{1}{j\omega C_s}} \tag{4}$$

The input equivalent impedance Z_{in} on the primary side is

$$\begin{aligned} Z_{in} &= R_{ps} + j\omega L_s + \frac{1}{j\omega C_{pp}} \bigg/\!\!\bigg/ \left(j\omega L_p + \frac{1}{j\omega C_{ps}} + R_p + Z_r\right) \\ &= R_{ps} + j\omega L_s + \frac{1}{j\omega C_{pp} + \frac{1}{Z_r + R_p + j\omega L_p + \frac{1}{j\omega C_{ps}}}} \end{aligned} \tag{5}$$

When the system operates at resonance, the simplified secondary side equivalent impedance Z_s, the secondary side equivalent impedance reflected to the primary side Z_r, and the primary side input equivalent impedance Z_{in} are given by

$$Z_s = R_s + R_L$$

$$
\begin{aligned}
Z_r &= \frac{\omega^2 M^2}{Z_s} = \frac{\omega^2 M^2}{R_s + R_L} \\
Z_{in} &= R_{ps} + \frac{\omega^2 L_{ps}^2}{Z_r + R_p} = R_{ps} + \frac{\omega^2 L_{ps}^2 (R_s + R_L)}{\omega^2 M^2 + R_p (R_s + R_L)}
\end{aligned} \tag{6}
$$

The primary side input current I_{in} of LCC-S is obtained as

$$
I_{in} = \frac{U_{in}}{Z_{in}} = \frac{U_{in}}{R_{ps} + \frac{\omega^2 L_{ps}}{R_p + Z_r}} = \frac{U_{in}[\omega^2 M^2 + R_p(R_s + R_L)]}{\omega^2 L_{ps}^2 (R_s + R_L) + R_{ps}\left[R_p(R_s + R_L) + \omega^2 M^2\right]} \tag{7}
$$

The current I_p flowing into the resonant coil on the primary side is

$$
I_p = \frac{\frac{1}{j\omega C_{pp}} \times I_{in}}{Z_r + R_p + j\omega L_p + \frac{1}{j\omega C_{ps}} + \frac{1}{j\omega C_{pp}}} = \frac{-j\omega L_{ps}(R_s + R_L)U_{in}}{(R_s + R_L)(\omega^2 L_{ps}^2 + R_{ps}R_p) + R_{ps}\omega^2 M^2} \tag{8}
$$

The secondary side output current value I_s of the LCC-S is

$$
I_s = \frac{j\omega M I_p}{R_s + R_L} = \frac{\omega^2 M L_{ps} U_{in}}{(R_s + R_L)(\omega^2 L_{ps}^2 + R_{ps}R_p) + R_{ps}\omega^2 M^2} \tag{9}
$$

The secondary side output voltage value U_o of the LCC-S is

$$
U_o = I_s R_L = \frac{\omega^2 M L_{ps} U_{in} R_L}{(R_s + R_L)(\omega^2 L_{ps}^2 + R_{ps}R_p) + R_{ps}\omega^2 M^2} \tag{10}
$$

Given that the parasitic resistance is typically of negligible magnitude, it can be reasonably disregarded in the analysis. Then the input current I_{in} on the primary side, the current I_p flowing into the resonant coil on the primary side, and the output current value I_s on the secondary side of the LCC-S are approximated as

$$
\begin{aligned}
I_{in} &\approx \frac{U_{in} M^2}{L_{ps}^2 R_L} \\
I_p &\approx \frac{-jU_{in}}{L_{ps}\omega} \\
I_s &\approx \frac{M U_{in}}{R_L L_{ps}}
\end{aligned} \tag{11}
$$

The output voltage U_o can be approximated as

$$
U_o \approx \frac{M U_{in}}{L_{ps}} \tag{12}
$$

From Equations (11) and (12), it can be observed that the LCC-S circuit exhibits constant current characteristics at the transmitter coil and constant voltage characteristics at the receiver coil. The output voltage U_o from the receiver coil is then fed into the subsequent DC/DC chopper circuit, following high-frequency rectification and filtering on the secondary side. Regarding the high-frequency rectification and filtering circuit, the following relationship holds between its input voltage U_{rec} and output voltage U_{dc}:

$$
U_{rec} = U_o = \frac{2\sqrt{2}}{\pi} U_{dc} \tag{13}
$$

Similarly, U_{dc} is the input to the subsequent DC/DC chopper circuit, with its value depending on the voltage induced by the receiver coil, which is related to the mutual inductance and typically in the hundreds of volts or more. The load, usually a battery, exhibits a voltage magnitude typically within the range of several tens of volts or below. To meet the voltage requirements, a BUCK converter is used for voltage reduction. A synchronous BUCK converter, which replaces the diode with a MOSFET, offers lower conduction losses and higher efficiency, making it suitable for achieving a constant voltage output.

3. Design of Sliding Mode Controller.

In this section, the mathematical model of the synchronous BUCK converter is derived and based on this, the SMC system of the synchronous BUCK converter is proposed, respectively. Finally, the stability of the designed SMC system is verified by proofs.

3.1. Mathematical modeling of synchronous BUCK converter.

The synchronous BUCK converter model is shown in Figure 4, where the pre-stage circuit is replaced by an equivalent DC source E. From Equation (13), $E = U_{dc}$, S_1 and S_2 are the MOSFETs, L is the energy-storage inductor, C is the output filter capacitance, R is the output load resistor, $i_L(t)$ is the inductor current, and V_o is the capacitor voltage. The system is second order due to the nonlinearity of the switching tubes and the presence of two energy storage elements in the circuit [30].

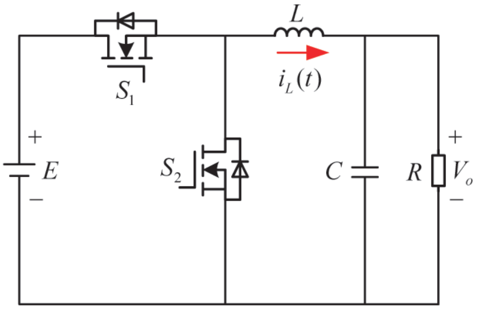

FIGURE 4. Circuit of synchronous buck converter

Assuming that the inductor current operates in Continuous Conduction Mode (CCM), when the S_1 is on and S_2 is off, the equivalent circuit model is shown in Figure 5. At this stage, the E stores energy for the inductor while simultaneously providing energy to the capacitor C and the load R, resulting the inductor current to increase, which is obtained according to Kirchhoff's voltage law:

$$\begin{aligned} \frac{di_L(t)}{dt} &= \frac{1}{L}(E - V_o) \\ \frac{dV_o(t)}{dt} &= \frac{i_L(t)}{C} - \frac{V_o}{RC} \end{aligned} \tag{14}$$

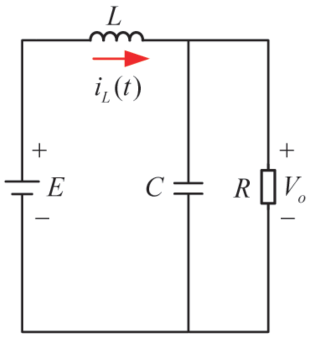

FIGURE 5. Circuit model when S_1 is on, S_2 is off

When the S_1 is off and S_2 is on, the equivalent circuit model is shown in Figure 6. At this stage the inductor acts as a power source to provide energy to the load R. The inductor current decreases and is obtained according to Kirchhoff's voltage law:

$$\begin{aligned} \frac{di_L(t)}{dt} &= -\frac{V_o}{L} \\ \frac{dV_o(t)}{dt} &= \frac{i_L(t)}{C} - \frac{V_o}{RC} \end{aligned} \tag{15}$$

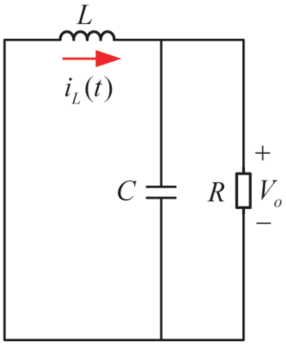

FIGURE 6. Circuit model when S_1 is off, S_2 is on

Assume that u is the input to the system and the output of the sliding mode controller. $u = 1$ means that the switch is on, and $u = 0$ means off. In fact, u is not a continuous input [31]. Then Equations (14) and (15) can be modified to the following relationship:

$$\begin{aligned} \frac{di_L(t)}{dt} &= \frac{1}{L}(uE - V_o) \\ \frac{dV_o(t)}{dt} &= \frac{i_L(t)}{C} - \frac{V_o}{RC} \end{aligned} \tag{16}$$

3.2. **Design of sliding mode controller.** The block diagram of the designed SMC system is shown in Figure 7, where E is the DC voltage source, S_1 and S_2 are the controlled MOSFETs, which are turned on and off by the PWM, L is the inductor, C is

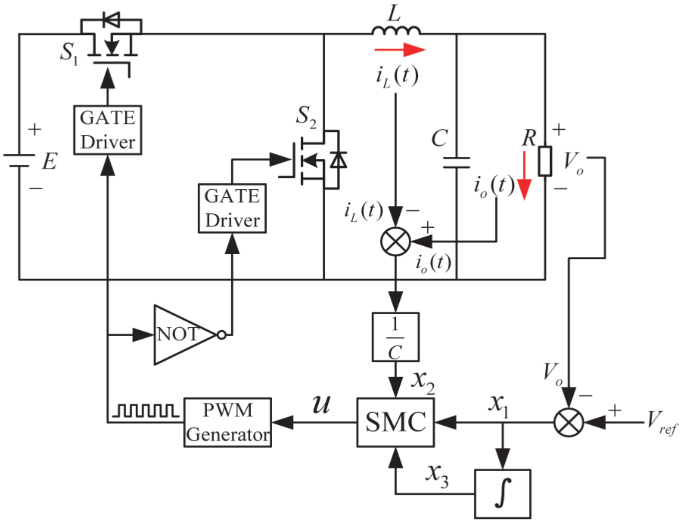

FIGURE 7. Block diagram of SMC system for synchronous BUCK converter

the capacitor, R is the resistor, V_o is the output voltage, $i_L(t)$ is the inductor current, and $i_o(t)$ is the resistor current.

The difference between the reference voltage V_{ref} and the load voltage V_o, i.e., the steady-state output voltage error, is chosen as the state variable x_1; the differentiation of the error is defined as the state variable x_2; and the integration of the error is defined as the state variable x_3. Then each state variable is denoted as

$$\begin{aligned} x_1 &= V_{ref} - V_o \\ x_2 &= \dot{x}_1 = -\frac{dV_o}{dt} = \frac{V_o}{RC} - \frac{i_L(t)}{C} = \frac{1}{C}(i_o(t) - i_L(t)) \\ x_3 &= \int x_1 dt \end{aligned} \tag{17}$$

Differentiating Equation (17) with respect to time t yields the required state space equations for the SMC system:

$$\dot{\boldsymbol{X}} = \boldsymbol{A}\boldsymbol{X} + \boldsymbol{B}u + \boldsymbol{D} \tag{18}$$

u means the control law.

Then,

$$\dot{\boldsymbol{X}} = \begin{bmatrix} \dot{x}_1 \\ \dot{x}_2 \\ \dot{x}_3 \end{bmatrix} = \begin{bmatrix} x_2 \\ -\frac{1}{LC}x_1 - \frac{1}{RC}x_2 - \frac{E}{LC}u + \frac{1}{LC}V_{ref} \\ x_1 \end{bmatrix} \quad \boldsymbol{A} = \begin{bmatrix} 0 & 1 & 0 \\ -\frac{1}{LC} & -\frac{1}{RC} & 0 \\ 1 & 0 & 0 \end{bmatrix}$$

$$\boldsymbol{X} = \begin{bmatrix} x_1 & x_2 & x_3 \end{bmatrix}^T \quad \boldsymbol{B} = \begin{bmatrix} 0 & -\frac{E}{LC} & 0 \end{bmatrix}^T \quad \boldsymbol{D} = \begin{bmatrix} 0 & \frac{V_{ref}}{LC} & 0 \end{bmatrix}^T$$

The sliding mode function can be made to be

$$S = k_1 x_1 + k_2 x_2 + k_3 x_3 \tag{19}$$

k_1, k_2, and k_3 are the sliding mode coefficients, all of which are positive. The sliding mode function governs the system's operating state, and an appropriately designed function ensures the system stays within the desired state. The next step is to design the control law u to direct the state variable trajectories toward the sliding mode surface and maintain their motion along it. The u is defined as follows [32]:

$$u = u_{eq} + u_n \tag{20}$$

where u_{eq} is called the equivalent control law and u_n is called the switching control law [33]. u_{eq} serves to maintain the running trajectory of the state variable along the sliding mode surface to the origin, and u_n serves to attract the running trajectory of the state variable to the sliding mode surface. The design of the u_{eq} can be obtained directly by making the derivative of the sliding mode function zero [34]:

$$\dot{S} = k_1 \dot{x_1} + k_2 \dot{x_2} + k_3 \dot{x_3} = 0 \tag{21}$$

Substituting Equations (17)-(20) into (21), the expression for the u_{eq} can be obtained as

$$u_{eq} = \frac{LC}{k_2 E}\left(k_1 x_2 - \frac{k_2}{LC}x_1 - \frac{k_2}{RC}x_2 + \frac{k_2}{LC}V_{ref} + k_3 x_1\right) \tag{22}$$

The u_n is generally a symbolic function and can be set to

$$u_n = \eta sign(S) \tag{23}$$

where η is the positive switching gain and $\eta > 0$. Therefore, the control law of the designed controller is

$$u = u_{eq} + u_n = \frac{LC}{k_2 E}\left(k_1 x_2 - \frac{k_2}{LC}x_1 - \frac{k_2}{RC}x_2 + \frac{k_2}{LC}V_{ref} + k_3 x_1\right) + \eta sign(S) \tag{24}$$

Next, the stability analysis of the designed SMC system is performed using the Lyapunov function. In general, the Lyapunov function is defined as [35]

$$V = \frac{1}{2}S^2 \tag{25}$$

where V is a positive definite function and for $S \neq 0$, there is $V > 0$ and $V(0) = 0$. The stability condition for the system can be expressed as

$$\dot{V} = S\dot{S} < 0 \tag{26}$$

or

$$\lim_{s \to 0^+} \dot{S} < 0 \cap \lim_{s \to 0^-} \dot{S} > 0 \tag{27}$$

Combining Equations (19)-(27) gives

$$\dot{V} = S\dot{S} = -S\frac{LC}{k_2 E}\eta sign(S) = -|S|\frac{LC}{k_2 E}\eta \tag{28}$$

For $S \neq 0$, Equation (28) less than zero is always valid. Therefore, the designed SMC system is stable [36].

4. Simulation Results.

4.1. Parameter setting.

Parameter setting. To verify the effectiveness of the designed SMC system, a simulation platform is built in Matlab/Simulink as shown in Figure 8. Simulations are conducted to compare the SMC system with traditional PI control under four operating conditions: start-up dynamics, reference voltage variation, load changes, and varying mutual inductance. The relevant circuit parameters are provided in Table 1.

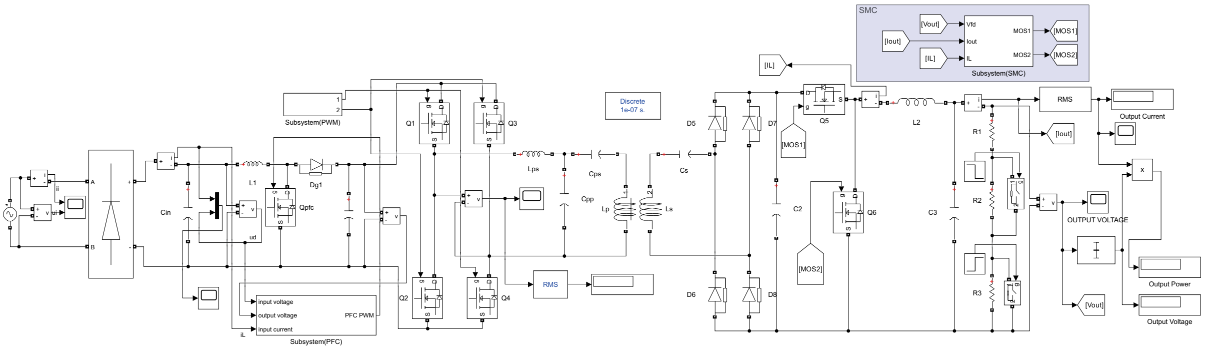

FIGURE 8. Proposed WPT system based on SMC modeled in Simulink

4.2. Start-up dynamics experiment.

Start-up dynamics experiment. The reference voltage V_{ref} is set to 52 V, the equivalent output load is 10 Ω, and the mutual inductance is 27 μH. As shown in Figure 9, when the system is controlled by sliding mode, the output voltage reaches the reference value from zero in approximately 2 ms, with a steady-state voltage error of 0.012 V and no overshoot. In contrast, with PI control, the output voltage takes about 12 ms to reach the steady state, the steady-state voltage error is approximately 0.36 V, and the system experiences an overshoot of around 17.3%.

TABLE 1. Parameters of the propoesd WPT system with SMC

Parameter	Description	Value
L_{ps}	Series resonant inductor on primary side	65 μH
C_{pp}	Parallel resonant capacitor on primary side	49 nF
C_{ps}	Series resonant capacitor on primary side	99 nF
C_s	Series resonant capacitor on secondary side	37 nF
L_p	Transmitter coil inductance	97.5 μH
L_s	Receiver coil inductance	84.5 μH
f	Resonant frequency	89 kHz
L_2	Synchronous BUCK converter inductor	1 mH
C_3	Synchronous BUCK converter capacitor	220 μF

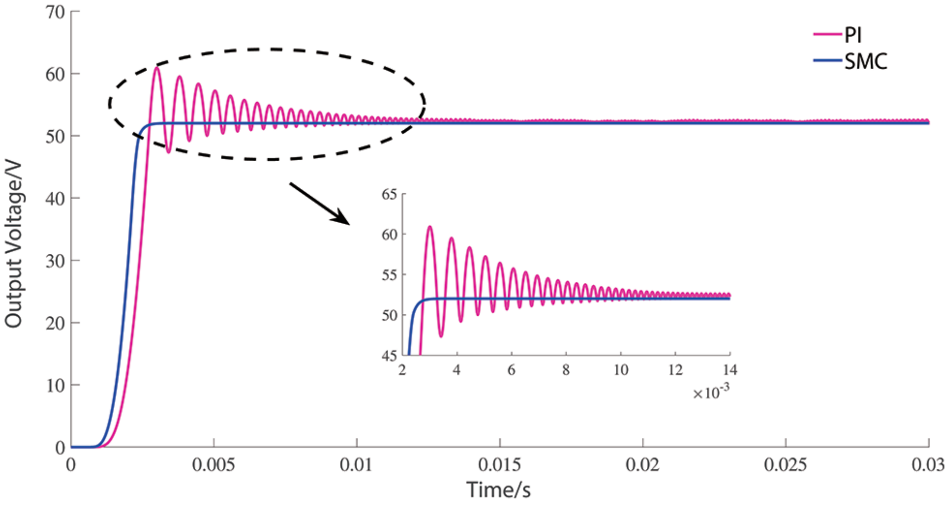

FIGURE 9. Start-up dynamic waveforms of PI control and SMC

4.3. **Reference voltage variation experiment.** To verify the performance of the output voltage following the reference voltage in the WPT system under SMC, a simulation experiment involving reference voltage variation is conducted. The equivalent output load is set to 10 Ω, the mutual inductance is 27 μH, and the reference voltage is changed from 52 V to 70 V at $t = 0.05$ s, then back from 70 V to 52 V at $t = 0.1$ s. Additionally, a comparison experiment with PI control is conducted under the same conditions.

As shown in Figure 10, the reference voltage changes from 52 V to 70 V at $t = 0.05$ s. When the system uses SMC, the output voltage responds from 52 V to 70 V in about 2 ms with no overshoot, and the steady-state voltage error is approximately 0.012 V. In contrast, with PI control, the output voltage takes about 10 ms to reach 70 V, experiences a nearly 20 V overshoot, and the steady-state voltage error is about 0.25 V.

As shown in Figure 11, the reference voltage changes from 70 V to 52 V at $t = 0.1$ s. When the system uses SMC, the output voltage responds from 70 V to 52 V in about 1.5 ms with no overshoot, and the steady-state voltage error is approximately 0.017 V. In contrast, with PI control, the output voltage takes about 10 ms to change from 70 V to 52 V, experiences nearly 13 V of overshoot, and the steady-state voltage error is about 0.28 V. It is evident that the designed controller offers faster response, smaller steady-state error,

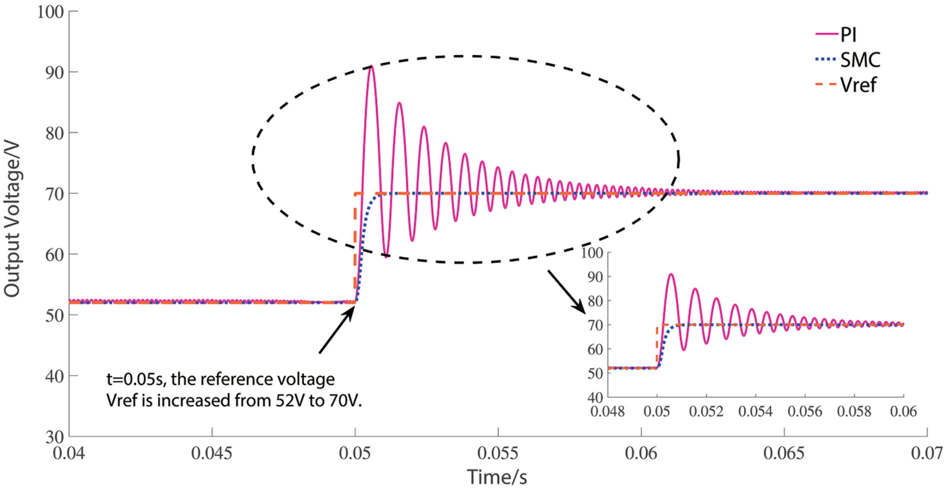

FIGURE 10. Reference voltage changes from 52 V to 70 V

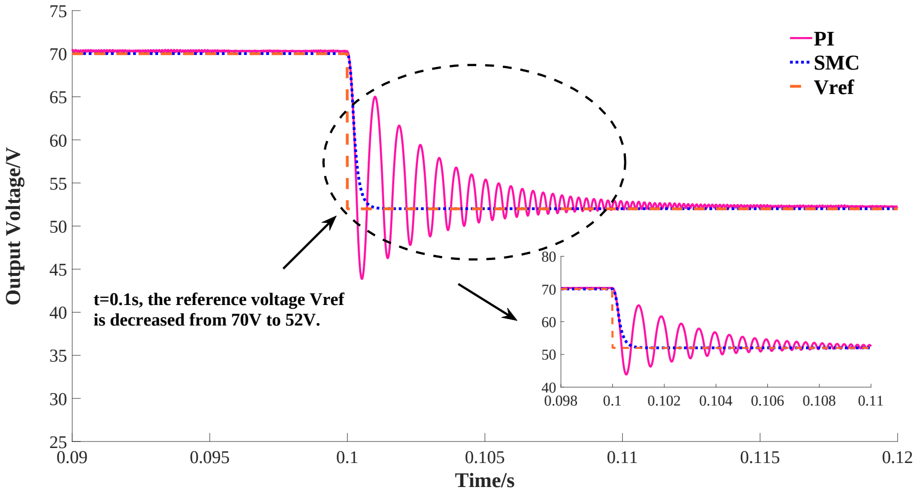

FIGURE 11. Reference voltage changes from 70 V to 52 V

and no overshoot, significantly improving the system's stability in the case of a sudden reference voltage change, compared to PI control.

4.4. **Load changes experiment.** To verify the robustness of the WPT system under SMC, a simulation experiment with sudden load changes is designed and conducted. The reference voltage is set to 52 V, the mutual inductance is 27 μH, and the initial load is 5 Ω. At $t = 0.03$ s, the load is increased to 15 Ω, and then reduced back to 5 Ω at $t = 0.06$ s. Additionally, a comparison experiment with PI control is conducted under the same conditions.

As shown in Figure 12, when the load is switched from 5 Ω to 15 Ω at $t = 0.03$ s, the system's response time is about 1 ms, with an overshoot of approximately 7 V, and the steady-state voltage error is around 0.02 V when using SMC. In contrast, when using PI control, the system's response time is about 10 ms, the overshoot remains around 7 V, and the steady-state voltage error is about 0.3 V.

When the load is switched from 15 Ω to 5 Ω at $t = 0.06$ s, the response time of the system with SMC is about 1 ms, with an overshoot of approximately 3.8 V, and the

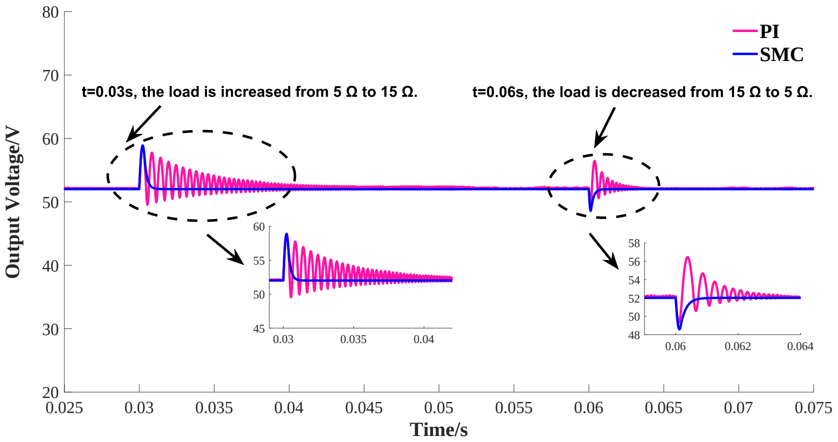

Figure 12. Response waveforms of the WPT system under load variations for SMC and PI control

steady-state voltage error is around 0.01 V. In contrast, with PI control, the system's response time is about 4 ms, the overshoot is about 4.5 V, and the steady-state voltage error is about 0.15 V. This comparison clearly shows that the designed SMC provides a faster response to sudden load changes, exhibits better overall robustness, and results in a smaller steady-state error compared to PI control.

4.5. **Varying mutual inductance experiment.** To verify the robustness of the WPT system under SMC when mutual inductance changes, a simulation experiment with sudden mutual inductance changes is designed and conducted. The equivalent output load is set to 10 Ω, and the reference voltage is 52 V. The output voltage is measured after the system reaches steady state, with data collected for mutual inductance values ranging from 10 μH to 40 μH. Additionally, a comparison experiment is conducted using PI control under the same conditions.

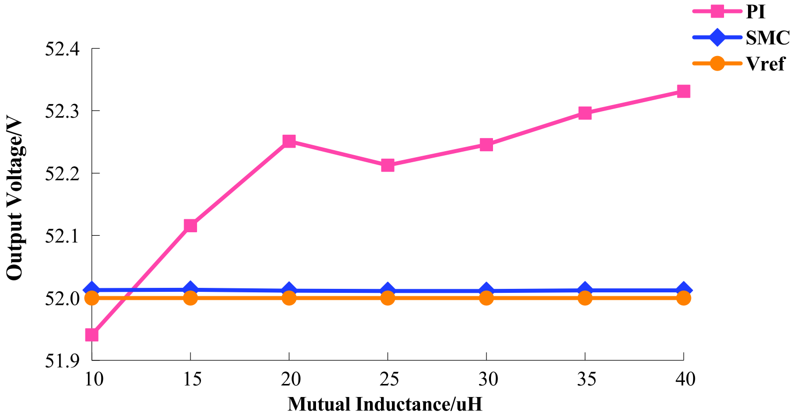

Figure 13. Steady-state output voltage vs. mutual inductance variation for WPT system under SMC and PI control

As shown in Figure 13, when the mutual inductance between the coils varies from 10 μH to 40 μH, the error between the steady-state output voltage and the reference voltage remains virtually constant at around 0.01 V under SMC, which is negligible. In contrast, when the system is controlled by PI, the error between the steady-state output voltage and the reference voltage becomes more noticeable. The error increases as the mutual inductance increases, reaching over 0.3 V when the mutual inductance is 40 μH, demonstrating that the control accuracy is significantly lower than that of the SMC.

5. **Conclusions.** To address the limitations of traditional PI control, characterized by slow response and low accuracy, this paper proposes a sliding mode controller based on the LCC-S and synchronous BUCK converter. This approach offers faster response, improved accuracy, and greater system robustness. Through analysis of the WPT system's structure, derivation of the mathematical model and state equations, definition of the sliding mode surface, and formulation of the control law, the proposed controller is validated via simulations. The results demonstrate superior performance in response speed, stability, and output accuracy compared to the traditional PI controller. In the future work, we will integrate parameter identification algorithms into sliding mode controller, dynamically optimizing controller parameters to enhance real-time performance and precision in constant voltage control.

Acknowledgment. This work is partially supported in part by the National Natural Science Foundation of China (Grant No. 62222307). The authors also appreciatively acknowledge the helpful suggestions and comments of the reviewers, which have improved the presentation.

REFERENCES

[1] Y. Zhang, Z. Shen, W. Pan, H. Wang, Y. Wu and X. Mao, Constant current and constant voltage charging of wireless power transfer system based on three-coil structure, *IEEE Transactions on Industrial Electronics*, vol.70, no.1, pp.1066-1070, 2023.

[2] W. Zhong and S. Y. Hui, Reconfigurable wireless power transfer systems with high energy efficiency over wide load range, *IEEE Transactions on Power Electronics*, vol.33, no.7, pp.6379-6390, 2018.

[3] X. Xie, C. Xie and L. Li, Wireless power transfer to multiple loads over a long distance with load-independent constant-current or constant-voltage output, *IEEE Transactions on Transportation Electrification*, vol.6, no.3, pp.935-947, 2020.

[4] Q. Zhang, C. Wang, H. Yuan, S. Zhang, J. Wang, D. Li and L. Yang, Research on input-parallel single-switch wireless power transfer system with constant-current and constant-voltage output, *IEEE Transactions on Power Electronics*, vol.37, no.4, pp.4817-4830, 2022.

[5] S. Pan, Y. Xu, Y. Lu, W. Liu, Y. Li and R. Mai, Design of compact magnetic coupler with low leakage EMF for AGV wireless power transfer system, *IEEE Transactions on Industry Applications*, vol.58, no.1, pp.1044-1052, 2021.

[6] Z. Yan, B. Song, Y. Zhang, K. Zhang, Z. Mao and Y. Hu, A rotation-free wireless power transfer system with stable output power and efficiency for autonomous underwater vehicles, *IEEE Transactions on Power Electronics*, vol.34, no.5, pp.4005-4008, 2019.

[7] Y. Yao, Y. Wang, X. Liu, Y. Pei, D. Xu and X. Liu, Particle swarm optimization-based parameter design method for S/CLC-compensated IPT systems featuring high tolerance to misalignment and load variation, *IEEE Transactions on Power Electronics*, vol.34, no.6, pp.5268-5282, 2019.

[8] X. Qu, Y. Jing, H. Han, S. C. Wong and K. T. Chi, Higher order compensation for inductive-power-transfer converters with constant-voltage or constant-current output combating transformer parameter constraints, *IEEE Transactions on Power Electronics*, vol.32, no.1, pp.394-405, 2017.

[9] K. Song, Z. Li, J. Jiang and C. Zhu, Constant current/voltage charging operation for series-series and series-parallel compensated wireless power transfer systems employing primary-side controller, *IEEE Transactions on Power Electronics*, vol.33, no.9, pp.8065-8080, 2018.

[10] C. Cai, S. Wu, Y. Zhang, J. Liu and S. Yang, Power transfer and control of wireless charging system based on an arc coil structure, *Transactions of China Electrotechnical Society*, vol.35, no.14, pp.2959-2968, 2020.

[11] Z. Li, C. Zhu, J. Jiang, K. Song and G. Wei, A 3-kW wireless power transfer system for sightseeing car supercapacitor charge, *IEEE Transactions on Power Electronics*, vol.32, no.5, pp.3301-3316, 2017.

[12] T. Tan, K. Chen, Q. Lin, Y. Jiang, L. Yuan and Z. Zhao, Impedance shaping control strategy for wireless power transfer system based on dynamic small-signal analysis, *IEEE Transactions on Circuits and Systems I: Regular Papers*, vol.68, no.3, pp.1354-1365, 2020.

[13] X. Wang, Y. Guo, R. Wang and Y. Zhang, Coordinated control of constant output voltage and maximum efficiency in wireless power transfer systems, *Applied Sciences*, vol.14, no.15, 2024.

[14] M. Kim, D. M. Joo and B. K. Lee, Design and control of inductive power transfer system for electric vehicles considering wide variation of output voltage and coupling coefficient, *IEEE Transactions on Power Electronics*, vol.34, no.2, pp.1197-1208, 2019.

[15] Y. Yenil and S. Cetin, Load independent constant current and constant voltage control of LCC-series compensated wireless EV charger, *IEEE Transactions on Power Electronics*, vol.37, no.7, pp.8701-8712, 2022.

[16] K. Chen, J. Pan, Y. Yang and K. W. E. Cheng, Stability improvement and overshoot damping of SS-compensated EV wireless charging systems with user-end buck converters, *IEEE Transactions on Vehicular Technology*, vol.71, no.8, pp.8354-8366, 2022.

[17] Z. Zhou, L. Zhang, Z. Liu, Q. Chen, R. Long and H. Su, Model predictive control for the receiving-side DC-DC converter of dynamic wireless power transfer, *IEEE Transactions on Power Electronics*, vol.35, no.9, pp.8985-8997, 2020.

[18] K. Chen, X. Yang, N. C. Cheung, E. K. W. Cheng and J. Pan, A communication-free fast constant current and voltage control method for dynamic wireless power transfer system, *IEEE Transactions on Industrial Electronics*, vol.72, no.3, pp.2455-2463, 2025.

[19] H. Zhang, Y. Chen, D.-H. Kim, Z. Li, M. Zhang and G. Li, Variable inductor control for misalignment tolerance and constant current/voltage charging in inductive power transfer system, *IEEE Journal of Emerging and Selected Topics in Power Electronics*, vol.11, no.4, pp.4563-4573, 2023.

[20] J. Peng, B. Zhang and W. Su, A hybrid control strategy of LCC-LCC compensated electric vehicles wireless charging system with wide ZVS range, *IEEE Transactions on Power Electronics*, vol.40, no.4, pp.6282-6295, 2025.

[21] W. Wang, J. Deng, D. Chen, Z. Wang and S. Wang, A novel design method of LCC-S compensated inductive power transfer system combining constant current and constant voltage mode via frequency switching, *IEEE Access*, vol.9, pp.117244-117256, 2021.

[22] H. Zhu, B. Zhang and L. Wu, Output power stabilization for wireless power transfer system employing primary-side-only control, *IEEE Access*, vol.8, pp.63735-63747, 2020.

[23] W. Zhang, W. Qin, J. Song, L. Lin and L. Bi, Development of constant current and constant voltage wireless charging system with mutual inductance identification function in primary side, *Electric Machines and Control*, vol.25, no.4, pp.52-60, 2021.

[24] F. Liu, K. Chen, Z. Zhao, K. Li and L. Yuan, Transmitter-side control of both the CC and CV modes for the wireless EV charging system with the weak communication, *IEEE Journal of Emerging and Selected Topics in Power Electronics*, vol.6, no.2, pp.955-965, 2018.

[25] B. Luo, L. Chen, Y. Li and R. K. Mai, Investigation of output voltage control for the inductive power transfer system based on sliding mode control theory, *Transactions of China Electrotechnical Society*, vol.32, no.23, pp.235-242, 2017.

[26] M. Wu, X. Yang, W. Chen, L. Wang, Y. Jiang, C. Zhao and Z. Yan, A dual-sided control strategy based on mode switching for efficiency optimization in wireless power transfer system, *IEEE Transactions on Power Electronics*, vol.36, no.8, pp.8835-8848, 2021.

[27] L. Wu, B. Zhang and Y. Jiang, Position-independent constant current or constant voltage wireless electric vehicles charging system without dual-side communication and DC-DC converter, *IEEE Transactions on Industrial Electronics*, vol.69, no.8, pp.7930-7939, 2022.

[28] L. Yang et al., Constant voltage and constant current control method of undersea wireless power supply system based on frequency tracking method, *IEEE Transactions on Power Electronics*, vol.40, no.4, pp.6359-6369, 2025.

[29] Z. Liu, L. Wang, Y. Guo and S. Li, Primary-side linear control for constant current/voltage charging of the wireless power transfer system based on the LCC-N compensation topology, *IEEE Transactions on Industrial Electronics*, vol.69, no.9, pp.8895-8904, 2022.

[30] S. M. RakhtAla, M. Yasoubi and H. HosseinNia, Design of second order sliding mode and sliding mode algorithms: A practical insight to DC-DC buck converter, *IEEE/CAA Journal of Automatica Sinica*, vol.4, no.3, pp.483-497, 2017.

[31] M. J. Deylamani, P. Amiri and M. H. Refan, Design and stability analysis of a discrete-time sliding mode control for a synchronous DC-DC buck converter, *International Journal of Control, Automation and Systems*, vol.17, no.6, pp.1393-1407, 2019.

[32] D. Matouk, F. Abdessemed, O. Gherouat and Y. Terchi, Second-order sliding mode for position and attitude tracking control of quadcopter UAV: Super-twisting algorithm, *International Journal of Innovative Computing, Information and Control*, vol.16, no.1, pp.29-43, 2020.

[33] K. Oyama, K. Hashikura, M. A. S. Kamal and K. Yamada, Two-step design method for sliding mode control to suppress spillover, *International Journal of Innovative Computing, Information and Control*, vol.18, no.6, pp.1841-1855, 2022.

[34] V. Repecho, N. Masclans and D. Biel, A comparative study of terminal and conventional sliding-mode startup peak current controls for a synchronous buck converter, *IEEE Journal of Emerging and Selected Topics in Power Electronics*, vol.9, no.1, pp.197-205, 2021.

[35] J. Guo, J. Cao, Y. Fu, Z. Ma, B. Li and D. Liu, Flow tracking of glue system based on non-singular terminal sliding mode active disturbance rejection control, *International Journal of Innovative Computing, Information and Control*, vol.16, no.5, pp.1757-1768, 2020.

[36] Y. Yue, X. Bai and X. Zuo, Friction compensation of electric control valve based on sliding mode with improved variable rate power reaching law, *International Journal of Innovative Computing, Information and Control*, vol.19, no.2, pp.403-418, 2023.

Author Biography

Wenzhou Lu received the B.Sc. degree in Electrical Engineering from Jiangsu University, Zhenjiang, China, in 2007, and the Ph.D. degree in Electrical Engineering from Southeast University, Nanjing, China, in 2013.

From February to August 2012, he was a Visiting Research Student with Nanyang Technological University, Singapore. He is currently an Associate Professor with the School of Internet of Things (IoT) Engineering, Jiangnan University, Wuxi, China. He has authored or coauthored more than 30 technical articles and patents in relevant areas. His research interests include power electronics and its control, renewable energy generation, and wireless power transfer technology.

Xu Wu received the B.S. degree in Electrical Engineering from Anhui Jianzhu University, Hefei, China, in 2022. He is currently working toward the M.S. degree in Electrical Engineering with the School of Internet of Things (IoT) Engineering, Jiangnan University, Wuxi, China. His research interests include wireless power transfer technology.

Yixin Zhu received the B.S., M.S., and Ph.D. degrees in Electrical Engineering from Xi'an Jiaotong University, Xi'an, China, in 2009, 2011, and 2015, respectively.

Since 2016, he has been with Jiangnan University, Wuxi, China, where he is currently with the School of Internet of Things Engineering as an Associate Professor. His research interests include the design, control, and application of the high-power active power filter, the photovoltaic grid-connected inverter, and also the modeling, analysis, and power management of the microgrid.

Tinglong Pan received his B.Eng. degree in Industrial Automation from China University of Mining and Technology, Xuzhou, China, in 1999, and the Ph.D. degree in Power Electronics and Power Drive from China University of Mining and Technology, Xuzhou, China, in 2004.

He is currently a Professor at Jiangnan University, China, where his research interests include microgrid control technology, power conversion technology, power drive system and its intelligent control technology.

Dezhi Xu received the Ph.D. degree in Control Theory and Control Engineering from Nanjing University of Aeronautics and Astronautics, China, in 2013.

He was a Visiting Fellow with the Department of Biomedical Engineering, City University of Hong Kong, Hong Kong, China, from 2018 to 2019. He is currently a Professor and Doctoral Supervisor with the Southeast University, China. His current research interests include data-driven control, fault diagnosis and fault-tolerant control, multi-agent systems and CPSs, technologies of renewable energy, motor control, and smart grid.

Dr. Xu was a recipient of the First Class Prize of Science and Technology Progression from the China General Chamber of Commerce in 2016, and the Best Young Scholar of Jiangnan University in 2022 for his research results. He is currently a Guest Editor or an Editorial Board Member for a number of journals, such as the International Journal of Innovative Computing, Information and Control, the Electric Power, the Zhejiang Electric Power, the Electrotechnical Application, and the Electrical Engineering. He is a Committee Member of the Association of Energy Internet, and Trusted Control in Chinese Association of Automation (CAA), and the Energy Storage in China Renewable Energy Society (CRES).